A. Growth mechanism of CHQ nanospheres and nanolenses

A1. Schematic of the growing mechanism

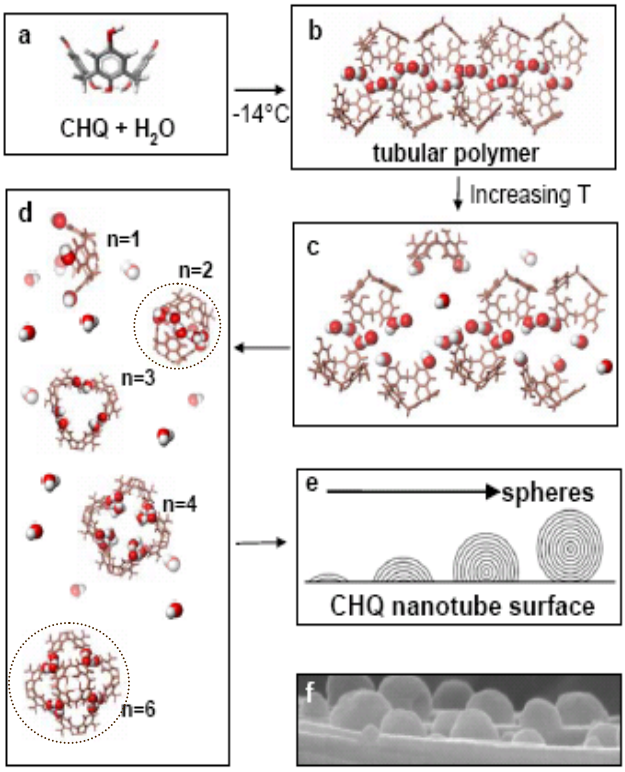

Figure S1 Schematic representation for self-assembling of CHQ nanostructures. **a**, Model structure of a monomer. **b**, Model structure of the strong hydrogen bond array composing the frameworks of CHQ nanotubes. The red and white balls denote the oxygen and hydrogen atoms of hydroxyl (-OH) groups forming the intermolecular hydrogen bonds. **c**, Model for temperature-induced breaking of the hydrogen bond array. **d**, Model structures of re-assembled small CHQ clusters. 'n' denotes the number of CHQ molecules. **e**. Scheme of growing lenses, hemispheres and spheres. **f**, SEM image of the hemispheres growing on the crystal surface.

Various self-assembled CHQ nanostructures[1] can be obtained by changing temperature and/or evaporation rate. The change of temperature can be a substantial factor to re-assemble a given CHQ nanostructure into another morphology. For instance, when CHQ nanotubes grown at -14℃ are heated at 40℃ in aqueous environments, the CHQ crystals become unstable. The CHQ molecules released from the destabilized crystals re-assemble into nanospheres consisting of dimer/hexamer-based units of CHQ. Besides raising

temperature, CHQ nanospheres may be assembled by allowing evaporation to occur for a week. Once the nanospheres are formed, they are stable both in aqueous and dry conditions and are resistant to temperature change up to ~ 150 ºC.

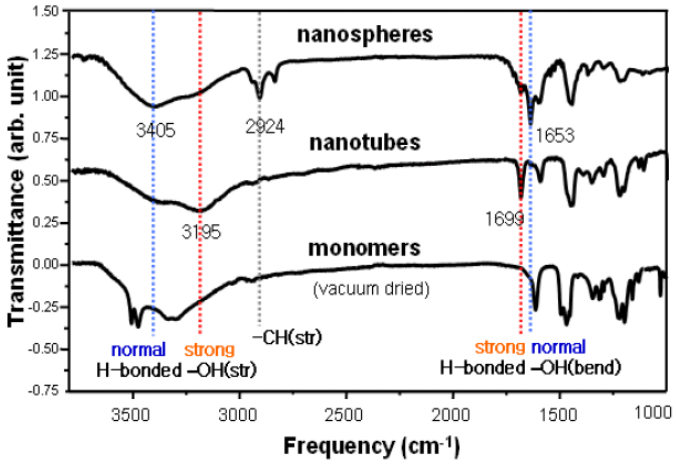

Figure S2 IR analyses of CHQ nanostructures.

In the IR spectra of CHQ nanospheres, the strong –OH stretching peak at ~3190 cm^{-1} originating from one-dimensional strongly hydrogen-bonded chains almost disappears (Fig. S2). This implies that the tubular frameworks of hydrogen bonds gradually disappear during conversion from nanotubes to nanospheres. Though the $–CH_2$ stretching peak around ~2900 cm^{-1} for nanotubes and monomers is very small, that for nanospheres is strong because the $–CH_2$ moieties of the dimer/hexamer are involved in π-H bonding with adjacent dimers/hexamers, which is consistent with the IR spectra of the CHQ nanospheres. In addition, the shift of hydrogen-bonded –OH bending peaks from ~1699 cm^{-1} to ~1653 cm^{-1} corresponds to the *ab initio* calculation[2] that hydrogen bonds of the dimer/hexamer-based assemblies are weaker than the one-dimensional hydrogen bonds of the nanotubes by ~3kcal/mol.

A2. Thermodynamical Analysis

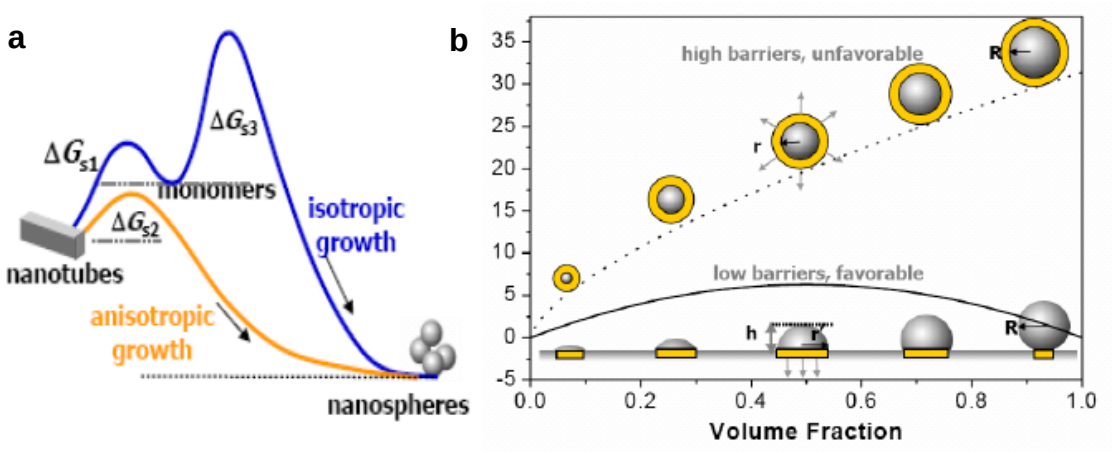

Figure S3 Proposed growth mechanism of CHQ nanospheres. **a**, A schematic representation of formation free energy profiles. **b**, Surface free energy barriers of isotropic/anisotropic growth with respect to volume fraction.

Interestingly, the CHQ nanospheres appear to be anisotropically springing from the hydrophobic surfaces of the CHQ nanotube crystals, while other types of nanospheres are known to grow through isotropic spherical expansions[3]. Therefore, the growing intermediates show interesting, partially spherical shapes. The CHQ nanospheres infrequently form directly from the supersaturated solution at room temperature, implying that isotropic growth of nanospheres is very slow because the spherical expansion costs substantial interfacial free energy compared to anisotropic growth (Fig. S3a).

To understand the anisotropic growth of the CHQ nanospheres, we propose a growth model (Fig. S3b). According to classical nucleation theory[4], the formation free energy (ΔG) depends on the free energy gained by the intermolecular interaction of transfering assembling units from liquid to solid (ΔG_V) and the free energy needed to create solid-liquid interfaces (ΔG_S):

$$\Delta G = \Delta G_V + \Delta G_S = V\rho_S\Delta\mu + A\gamma \quad \text{(for spherical assemblies) (S1)}$$

where V is the volume of nanospheres, $\Delta\mu$ (<0) is the difference in chemical potential of the solid and the liquid, A is the surface area for growth and γ is the interfacial free energy density. In the case of equal volumes, spherical shapes with minimum surface area are always thermodynamically most stable. However, their growth rate depends more on the actual surface area of growth where incoming molecules form an additional layer on the surface, which can be described as:

$$A_i = 4\pi r^2 \qquad \text{(for isotropic growth of a sphere)} \qquad \text{(S2)}$$

$$A_a = \pi r'^2 \qquad \text{(for anisotropic growth of a sphere)} \qquad \text{(S3)}$$

where r is the radius of the intermediate spheres and r' is the radius of the area in contact with the crystal surface (Fig. S3b). The interfacial free energies for isotropic growth and anisotropic growth can be represented as a function of volume fraction under the assumption that γ is not significantly different for anisotropic and isotropic growth. The graph shows that the interfacial free energy of isotropic growth is larger than that of anisotropic growth. Therefore, anisotropic growth is always kinetically favorable, though the isotropic intermediates are always thermodynamically more stable. The schematic representation in Fig. S3a summarizes the formation process of CHQ nanospheres. The direct formation of CHQ nanospheres from solvated monomers is unfavorable because of the high interfacial free energy barriers for isotropic growth. Instead, the monomers crystallize into CHQ nanotube crystals first and then follow the low-energy barrier path of anisotropic growth to form CHQ nanospheres.

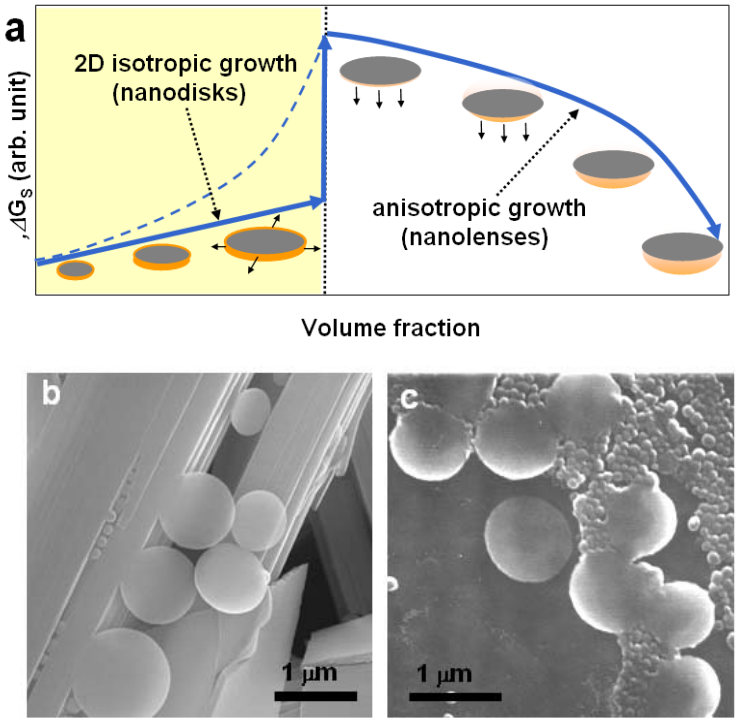

Figure S4 a, Schematic representation of the surface free energy barrier of growing CHQ nanolenses. **b**, A SEM image of CHQ lenses attached to CHQ nanotube crystals. **c**, A SEM image showing the morphology conversion from CHQ nanolenses to spheres.

The film-like structures of CHQ often cover the surface of CHQ crystals. In this case, the CHQ molecules released from the surface of crystals cannot diffuse into solution directly. Instead, they are concentrated within a small volume under the film, which induces high chemical potentials ($\Delta\mu$) leading to fast nucleation and kinetic growth of disk-shaped structures (Fig. S4a, left). At lower temperatures around −10°C, the disks seem to grow kinetically even without the assistance of film structures. Then, the spherical curvatures are formed as the released CHQ molecules take part in the self-assembly (Fig. S4a, right). The growing surface areas for disks and lenses can be represented respectively as:

$$A_i' = 2\pi R \cdot t \qquad \text{(for 2D isotropic growth of a disk)} \qquad \text{(S4)}$$

$$A_a' = \pi R'^2 \qquad \text{(for anisotropic growth of a lens)} \qquad \text{(S5)}$$

where R and t are the radius and thickness of the disk, respectively, and R' is the radius of the growing surface area in contact with the crystals. Since A_i' is much smaller than A_a', the disk grows faster than the lens, and then it reaches its equilibrium size. Thus, the overall growth process results in the formation of a "Plano-Convex" type of lens with near-perfect spherical curvature, which is stable once it is isolated and dried in the air (Fig. S4b). However, if not isolated from aqueous solution, the CHQ nanolenses are dynamically converted into CHQ nanospheres in 2~3 days at room temperature (Fig. S4c), implying the nanospheres are the most stable CHQ nanostructures.

B. Near-Field Optics of a Nanolens

B1. Comparison between ray-tracing and FDTD simulation for a nanolens

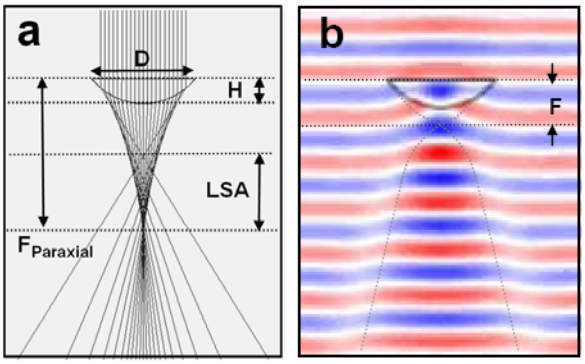

Figure S5 a, A Ray-tracing simulation result of the lens calculated by OSLO program packages (Sinclair Optics, Inc.). **b**, A finite-difference time-domain (FDTD) simulation result (E_x) obtained by FullWAVE 4.0 program (RSoft Design Group). D = 800nm, H = 280 nm and λ=365 nm.

When the size of optical elements is much larger than the wavelengths of light, wave-like features such as interference and diffraction are negligible, and the optical phenomena can be described by geometrical far-field optics. In this limit, optical imaging through plano-spherical convex (PSC) lenses can be simply simulated by ray-tracing methods based on Snell's law (Fig. S5a). The paraxial focal length ($F_{paraxial}$) of a PSC lens is described as $F_{paraxial} = R / (n\text{-}1)$, where R is the radius of curvature and n is the index of refraction. As the lens size decreases to the wavelength, the interference between the incoming and refracted waves is more important, and the interactions between the lens and the propagating electromagnetic (EM) waves need to be understood from the accurate solution of Maxwell's equation (Fig. S5b). As a result, the substantial difference between the far-field geometrical optics and the near-field wave optics is shown in their focal lengths. The focal length F obtained from EM wave simulations is found to be much shorter than $F_{paraxial}$ obtained from the ray tracing method. This reduced focal length in the CHQ nanolens implies enhanced magnifying effects through the near-field objective lenses.

B2. Focusing behavior of a nanolens

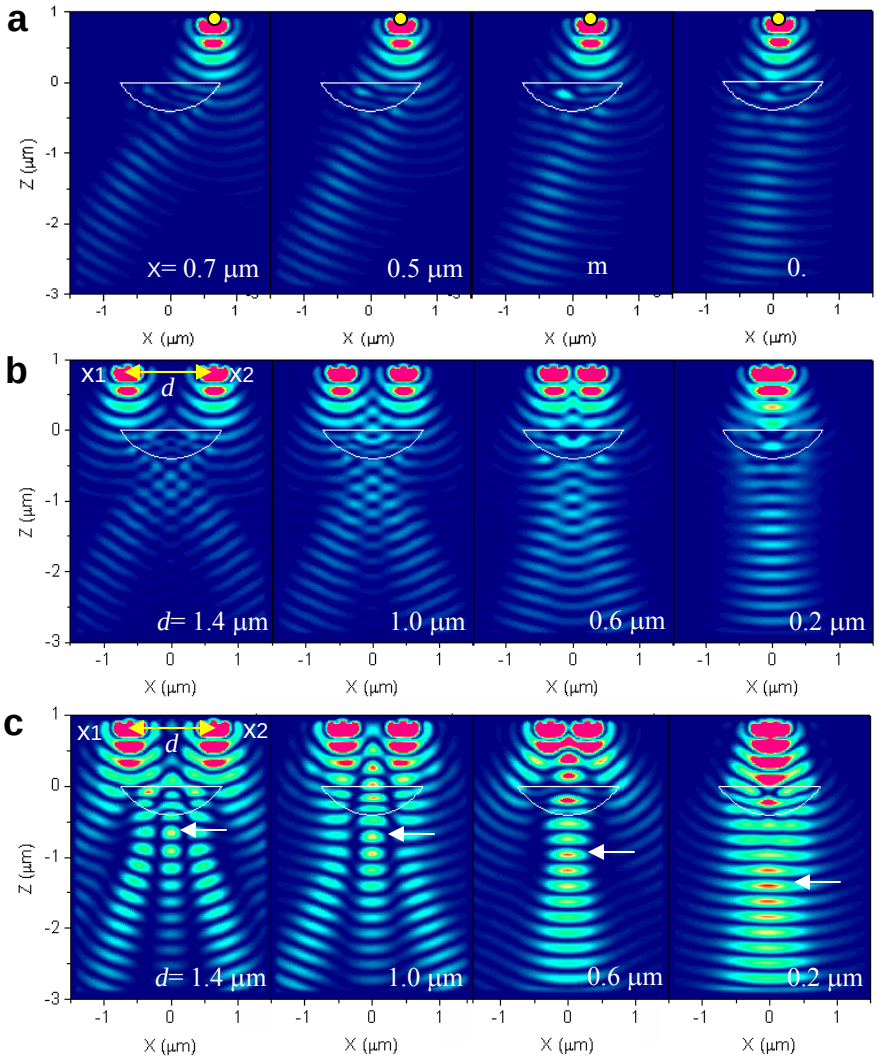

Figure S6 FDTD simulation results of light intensities ($|E_x|^2$) through a CHQ lens using point sources at different positions (x=100~700nm). D=1.5μm, H=0.4 μm and λ=472 nm. **a,** Change of refracted angle depending on the position of a light source. **b**, Simple sum of two wave intensities from each source, assuming that the waves are independently propagating without interference ($|E_x|^2 = |E_{x1}|^2 + |E_{x2}|^2$). **c**, Intensities of two interfering waves through the lens ($|E_x|^2 = |E_{x1} + E_{x2}|^2$). The arrows denote the highest-intensity spots.

It is known that the asymptotic limit (Rayleigh limit) of the diffraction of light through a lens for short wavelengths is refraction. Here, we investigate the optical

properties of refraction and diffraction of the beam-like light sources through the nanolens (Fig. S6). The single light source simulation (Fig, S6a) deceptively appears to be a refraction-like pathway at first sight. However, careful analysis shows that the pathway is much more tortuous than the geometrical ray path. This is due to the fact that at the interface between the inside and outside of the convex nanolens having extremely high curvature, the wave path must be strongly twisted to match the phase of the wave front inside the lens with that outside the lens (Fig. S6a). The beam pathways visualized along the highest intensity profiles in Fig. S6b shows the case where the intensities of two symmetric waves are simply added. However, the actual intensity is formed by the interference of two waves from each source, where each of the brightest spots can be considered a focal point (Fig. S6c). In this case, the intensity increases due to the enhancement of the amplitude by superposition (i.e., the diffraction effect), as compared with the case of Fig. S6b. The focal length tends to be much smaller for the light sources closer to the edges of the lens. Since the solid angle around the edges is much larger than that around the center, the focal length obtained by the plane wave is close to the focal length obtained by the two symmetric sources near the edges. Since this focal length is much shorter than that obtained by the geometric ray tracing, the focusing phenomenon by a nanolens is due to the near-field focusing whose origin arises from the stringent phase matching phenomenon at the interface of a nanolens with extremely large curvature.

C. Magnifying effects of the CHQ nanolens

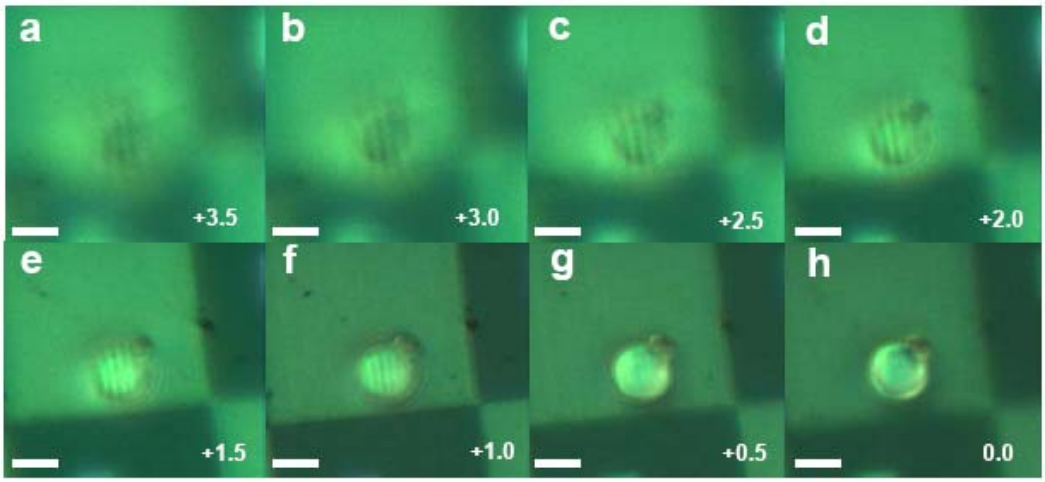

Figure S7 Reflection mode optical microscope images of a nanolens showing the magnified images of underlying objects (250 nm pitch stripe patterns), corresponding to the SEM image in Fig. 2b. The numbers indicate the relative distance (in μm) from the top of the lens. Lens dimension: D=~2.7 μm, H=~0.8μm (scale bars, 2μm).

Figure S7 shows the magnification effects obtained through the nanolenses, with the images taken from the different distances from the top of face-up CHQ lens. Fig. S8a shows magnification as large as 2.5. Also, the face-up CHQ lens shows pincushion distortion that also appears in geometric lenses (Fig. S7a-d), which is not seen in the face-down CHQ lens.

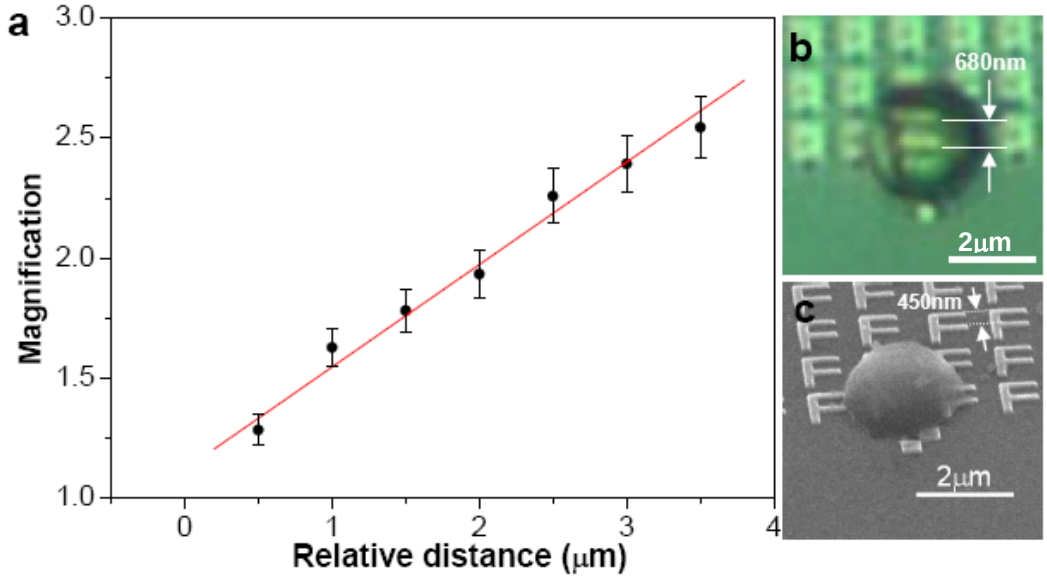

Figure S8 Magnifying Effects through CHQ nanolenses. **a,** Magnification with respect to the relative distance from the top of lens obtained from Fig. S5. The error bars denote s.d. **b-c,** OM/SEM images of the CHQ lens on the 'F' patterns. The line spacing looks magnified by ~1.5 through the lens.

D. Negative e-beam resist properties of CHQ nanostructures

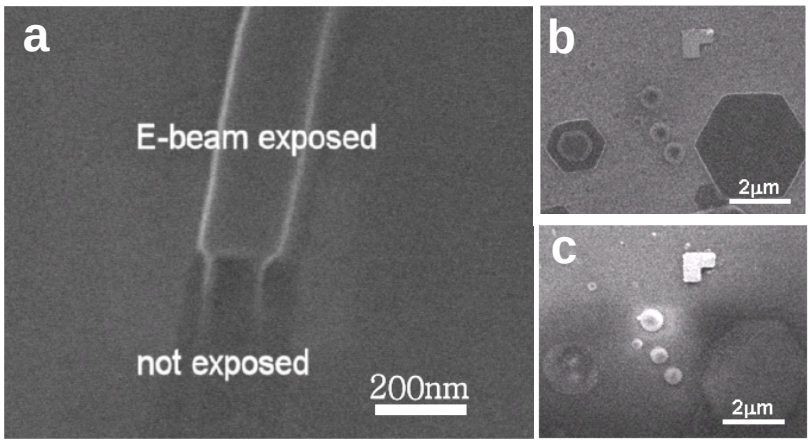

Figure S9 a, A SEM image of CHQ nanotube dissolved in developer (isopropyl alcohol (IPA) : water = 1 : 3) after being exposed to an electron beam. **b-c**, SEM images of CHQ structure before (b) and after (c) exposure. CHQ hexagonal plate which are not exposed to electron beam are dissolved in the developer, while e-beam exposed CHQ nanolenses are dissolved.

CHQ nanostructures consisting of the CHQ monomers with calixarene-based structures may be useful as an electron beam negative resist. After a CHQ nanostructure is exposed to an electron beam, only the unexposed portion of the CHQ nanostructure is dissolved in 1:3 IPA-water solution as a developer (Fig. S9). The selective exposure of CHQ based structures to an electron beam can then be used to control the size and position of CHQ nanostructure. This can be used for precise fabrication of nano-electric and optical devices utilizing CHQ nanostructures including nanolenses (Fig. S9b-c).

E. Relocation of CHQ nanolenses for fabrication

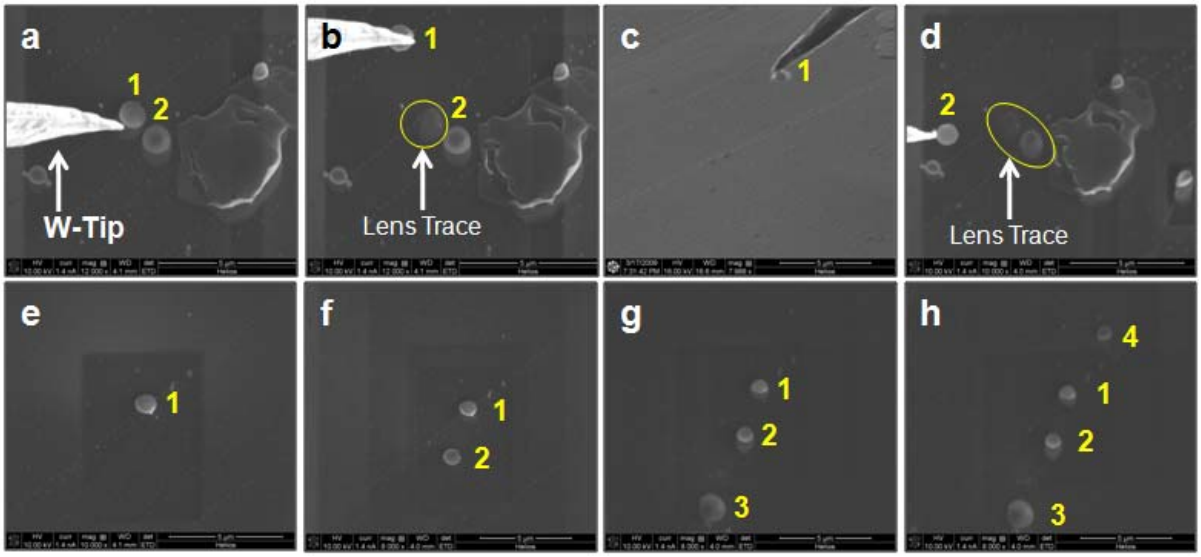

Figure S10 FIB-SEM/SIM-images to demonstrate transfer of CHQ nanoscale lenses by the Dual FIB technique. **a**, tip approaching a nanoscale lens 1. **b**, tip which picked up lens 1. **c,** transfer of lens 1 by the tip. **d**, tip which picked up lens 2. **e**~**h**, four CHQ nanolenses 1-4 which are arranged as a linear array one by one.

The ability to transfer nanomaterials is very important for fabrication in nanotechnology. We have demonstrated the transfer of CHQ nano-scale lenses using a dual focused ion beam (FIB) technique, as in Fig. S10. To take CHQ nanoscale lenses off the surface, we used the tungsten (W) tip. The top of the tip is first painted with adhesive by pushing the tip into the adhesive of adhesive carbon tape. The transfer of a CHQ nanoscale lens was performed with direct observation of the SEM-image at the vertical angle (0^o) and the scanning ion microscope (SIM)-image at the tilted angle (52^o). The SEM-images were taken at 10 kV and 1.4 nA (probe current), and the SIM-images, at 16 kV and 21 pA. In the beginning, we moved two lenses of equal size, each with diameter of 1.0 μm, demonstrating that we are able to arrange equal size lenses as an array. Then, we moved a slightly large lens with diameter of 1.6 μm, followed by a slightly small lens with diameter of 0.8μm. In this way, we have shown that the nanoscale lenses can be

manipulated. The tip in FIB can be employed to take each nanolens off the surface and put it at a pre-determined position. Lenses of either uniform size or non-uniform size for a specific purpose can be selected. Thus, it is possible to make any kind of shapes as well as arrays. A simple demonstration of an array comprised of four nanolenses, two of almost equal size, one of larger size, and one of smaller size is provided in Fig. S10. In Fig. S10d, one can note that the nanoscale lens is on the top of the tip, which indicates that it would enhance the resolution of aperture-less near-field scanning optical microscope (ANSOM). Indeed, to demonstrate this more vividly, another experiment has been carried out, as in Fig. S11. Here, the CHQ lens is transferred to the top of an AFM tip. A blunt W tip is used to detach the CHQ lens from the substrate for the transfer of the CHQ lens.

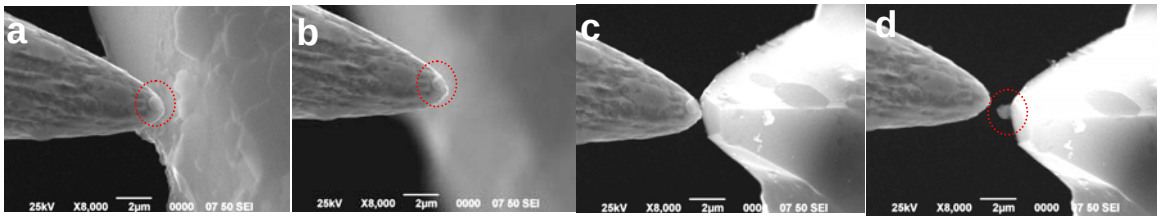

Figure S11 SEM images demonstrating transfer of a CHQ lens to the top of an AFM tip **a**, attaching a CHQ lens on the substrate to a W tip. **b**, a SEM image of the CHQ lens on the W tip. **c,** transferring the lens on the W tip to the top of the AFM tip. **d**, CHQ lens on the top of the AFM tip.

F. Pattern of palladium lines on the Si surface in Figure 3

The pattern in Fig. 3 is different from that in Fig. 2. In Fig.2, the pattern is 10μm x 10μm, with very fine lines of 220nm and 250nm pitch and 77~80nm width (in SEM images). The pattern in Fig.3 is 1μm x 2μm and has 5 lines with ~200nm pitch and 100nm width. In the "in focus" image in Fig.3c, the 5 lines were not resolved without nano-scale lenses, but they were seen as a single short stripe.

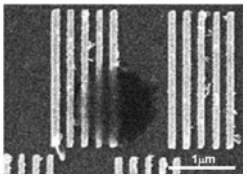

Figure S12 Pattern of the palladium lines which were used in Fig. 3c.

G. UV lithography using a nanoscale lens

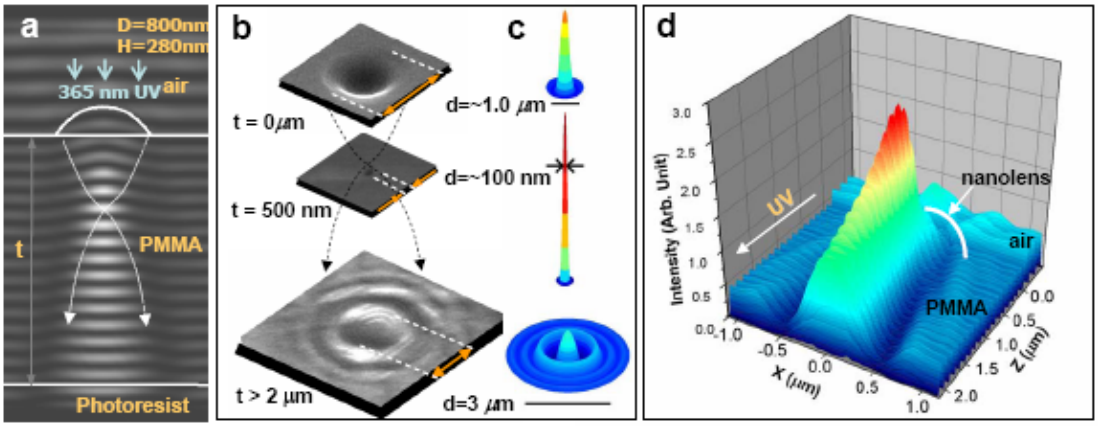

Figure S13 Photochemical imaging through the CHQ lenses. **a**, A FDTD simulation image ($|E_x|^2$) of the lens on resist polymer layers. The distance between the lens and the photoresist can be adjusted by changing the thicknesses of the PMMA layers. **b**, SEM images of developed patterns after irradiating 365nm UV light through the nanolenses, showing the focused spot as small as 100nm and the increased focal length in the polymer resists. The refractive indices of PMMA and AZ5124E photoresist layers are 1.49 and 1.64, respectively. The UV exposure time is 1s for t=0 ~500nm, and 4s for t>2μm. The developing time in AZ400K:H_2O 1:4 solution is 8s. **c**, FDTD simulation images corresponding to b. **d**, Electric field intensity profiles ($|E_x|^2$) corresponding to a, showing sharp peaks at F=500~600 nm.

Near-field focusing with CHQ nanolenses can be utilized for nanometer scale lithographic applications. We carry out photochemical lithography using λ = 365nm ultraviolet (UV) light to confirm the reduction of focal lengths by near-field lens refraction. The distance between the lens and the photoresist (PR) layer (t) is adjusted by coating PMMA layers with different spinning rates and concentrations (Fig. S13a). Similar sizes of the lenses (D=0.8~1 μm, H = 200~300 nm) are used to focus the UV light through the PMMA layers of different thicknesses. The sample was exposed to 85W UV light, and developed with AZ400K:H_2O 1:4 solution. The PMMA layers are lifted off as the developer dissolves the exposed photoresist layers. The CHQ lenses can be easily removed because CHQ is soluble in the developer. Even with aberrations, the results show that focused spots as small as 100 nm (Abbe limit ~ 192 nm in air and ~ 115 nm in

oil) are formed with a 500 nm-thick spacer, while a few μm-wide ring diffraction patterns are formed as the thickness increases over ~2 μm (Fig. S13b). In the case of CHQ nanolenses in contact with the photoresist layer, ~1 μm-wide and ~500 nm-deep wells are formed (instead of sharp spots or diffraction rings). This indicates that the focal lengths increase inside the polymer resists because of the larger refractive index of medium (n_{PMMA} =~1.5, n_{PR} =~1.6). This result is consistent with the EM wave simulation results (Fig. S13c,d), though nonlinear effects may also need to be considered to achieve quantitative agreement. Indeed, such nonlinear effects could be utilized to make a smaller spot size as the exposing time is reduced.

H. Single near-infrared photon spectroscopy

In near-infrared (1.55μm) spectroscopy, detection of single photons from single narrow-band-gap quantum dots has been a major milestone for quantum key distribution and quantum information processing. The 1.55μm wavelength region is especially important due to its direct compatibility with the embedded optical fiber network. The challenge, even with state-of-the-art low-dark-count InP/InGaAs single photon detectors, is the collection efficiency above the noise. This challenge can be addressed with CHQ nanolenses especially with the AFM and ANSOM positioning capabilities.

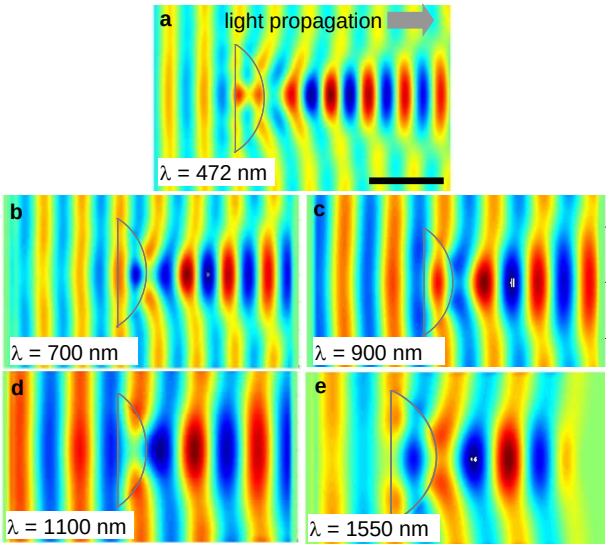

Figure S14 FDTD modeling of nanolenses focusing at different wavelengths. **a-d**, Lens dimension: D=~2.7 μm, H=~0.8μm; and **e**, Lens dimension: D=~5.4 μm, H=~1.6μm (scale bars, 1μm).

As an example, it is possible to perform micro-photoluminescence measurements with these nanolenses for enhanced photon collection efficiency from near-infrared PbS colloidal quantum dots. In this case, the complete numerical simulations without any

approximations (FDTD simulations) in Fig. S14 show that the lens focuses the near-infrared photons from the dipole emitter into a distinct propagation cone (instead of all 4π steridians). This can then be matched by the objective of a confocal microscope for significantly enhanced photon counts, supporting efforts to detect single quantum emitters at telecommunications wavelengths. The detection of single near-infrared photons through these nanolenses would be a major advance for scalable quantum information processes. The nanolens can also help in near-infrared micro-photoluminescence spectroscopy, where improved collection efficiency is critical.

I. Enhancement of micro-Raman intensity using nanolenses

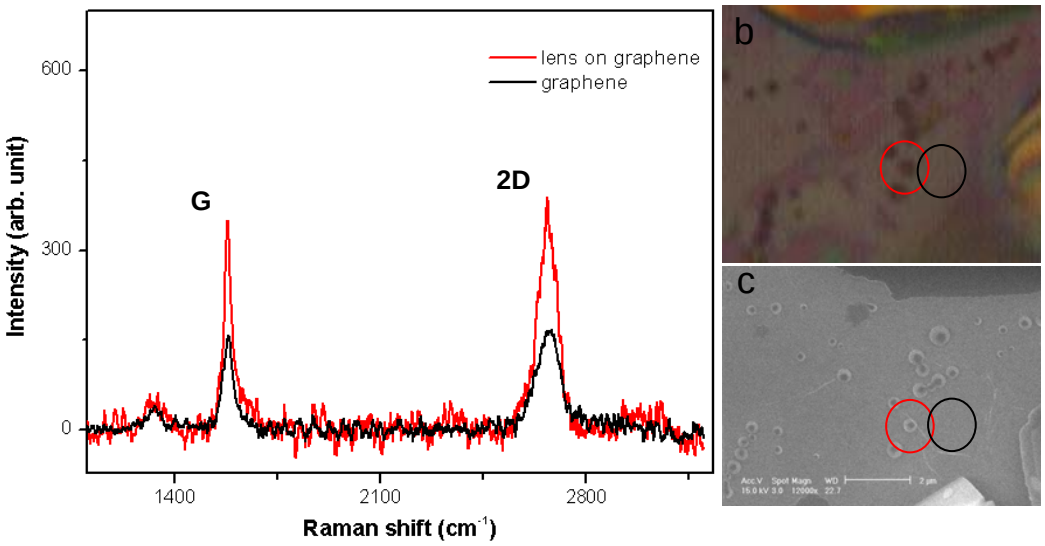

Figure S15 Micro-Raman spectra of a CHQ lens on graphene. **a**, Raman spectrum of the graphene without the CHQ lens (black) and that with the CHQ lens (red), where the baselines of the spectra are removed. **b-c,** An OM image (b) and a SEM image (c) of CHQ lenses deposited on graphene. The red and black circles represent the positions where the Raman spectra were obtained.

Raman spectroscopy is an important tool for identifying and analyzing molecules. However, due to the low scattering cross-section, Raman spectroscopy is often performed in configurations that allow for signal enhancement, such as surface-enhanced Raman scattering (SERS) that relies on the use of nanoscale metal structures.[5] We have observed Raman spectra using Micro-Raman spectroscopy in which a laser beam is focused onto a CHQ lens and the Raman signal through the CHQ lens on graphene is detected. The wavelength and power of the laser are 633 nm and 4 mW, respectively. Fig. S15 shows that the G and 2D peaks of graphene are enhanced through the CHQ lens, as the lens collimates and focuses the scattered Raman signal from the graphene. In addition, the spatial resolution of Raman microspectroscopy is expected to be enhanced by using the CHQ lens, since the CHQ lens has shown remarkable resolution in the visible and UV regions.

J. Supplementary References

1. Hong, B. H., Lee, J. Y., Lee, C.-W., Kim, J. C., Bae, S. C. & Kim, K. S. Self-assembled arrays of organic nanotubes with infinitely long one-dimensional H-bond chains. *J. Am. Chem. Soc*. **123**, 10748-10749 (2001).

2. Kim, K. S. *et al.* Assembling phenomena of calix[4]hydroquinone nanotube bundles by one-dimensional short hydrogen bonding and displaced π-π stacking. *J. Am. Chem. Soc*.**124**, 14268-14279 (2002).

3. Ding, L. & Olesik, S. V. Synthesis of polymer nanospheres and carbon nanospheres using themonomer 1,8-dihydroxymethyl-1,3,5,7- octatetrayne. *Nano Lett*. **4**, 2271-2276 (2004).

4. Auer, S. & Frenkel, D. Prediction of absolute crystal-nucleation rate in hard-sphere colloids. *Nature* **409**, 1020-1023 (2001).

5. Hartschuh, A., Anderson, N. & Novotny, L. Near-field Raman spectroscopy using a sharp metal tip. *J. Microsc.* **210**, 234-240 (2003).